electronics

MDPI

Article

Resonance Capacitance Selection Method for Minimizing Leakage Magnetic Fields and Achieving Zero Phase Angles in Wireless Power Transfer Systems

Yujun Shin [1], Jaewon Rhee [2] and Seongho Woo [2,*]

[1] Automotive Engineering, Department of Smart Mobility Engineering, Keimyung University, Daegu 42601, Republic of Korea; yjshin@kmu.ac.kr
[2] Cho Chun Shik Graduate School of Mobility, Korea Advanced Institute of Science and Technology, Daejeon 34051, Republic of Korea; elly0386@kaist.ac.kr
* Correspondence: seongho@kaist.ac.kr

Abstract: This study proposes a novel approach for selecting the resonance capacitance of wireless power transfer systems, aiming to achieve a zero phase angle (ZPA) while simultaneously minimizing the leakage magnetic field. The performance of the method is validated across two key topologies: series–series (S–S or SS) and the double-sided inductor–capacitor–capacitor (LCC, LCC–LCC) topologies. By minimizing the vector phasor sum of the coil currents, the proposed approach effectively mitigates magnetic field leakage. The method is further validated through mathematical derivations, simulations, and experimental tests. The results reveal that using the proposed method to select resonance capacitances reduces the leakage magnetic field by up to 35.2% in the SS topology and by 42.0% in the double-sided LCC topology. Furthermore, the method improves the ZPA by more than 20° in both cases. These outcomes affirm the effectiveness of the proposed resonance tuning approach.

Keywords: wireless power transfer; magnetic field; resonance circuits; zero phase angle; topology; electric vehicle

Citation: Shin, Y.; Rhee, J.; Woo, S. Resonance Capacitance Selection Method for Minimizing Leakage Magnetic Fields and Achieving Zero Phase Angles in Wireless Power Transfer Systems. *Electronics* **2024**, *13*, 4188. https://doi.org/10.3390/electronics13214188

Academic Editor: François Auger

Received: 21 September 2024
Revised: 20 October 2024
Accepted: 23 October 2024
Published: 25 October 2024

1. Introduction

Wireless power transfer (WPT) systems have garnered considerable attention owing to their potential for widespread application across diverse industries [1,2]. The ability of WPT systems to deliver energy without requiring physical connections makes them particularly suitable for use in electric vehicle chargers, medical devices, consumer electronics, and industrial automation systems [3–5]. The convenience and safety advantages offered by WPT systems, along with their potential to revolutionize power delivery in these fields, have spurred considerable research interest. Consequently, extensive research is ongoing to address existing technical challenges and enhance the performance, power transfer efficiency (PTE), and reliability of WPT systems, ultimately aiming to facilitate their widespread adoption across diverse applications [6,7].

One of the key challenges encountered by WPT systems is the issue of leakage magnetic fields, which originate from the magnetic fields used for energy transfer [8,9]. These unintended fields can extend beyond the designated energy transfer area, potentially interfering with the fields of nearby electronic devices and hence raising safety concerns. These leakage magnetic fields not only diminish the PTE of the WPT system but also complicate its practical implementation, particularly in environments requiring electromagnetic compatibility. Hence, minimizing these leakage fields has become a central focus of research on the design and optimization of WPT systems.

In addition to addressing leakage magnetic fields, it is crucial to tune the resonance of the WPT system for optimal operation [10–12]. Specifically, zero phase angle (ZPA) [12–14]

and zero voltage switching (ZVS) [15] are important factors in achieving high PTE. A ZPA is achieved when the input impedance of the WPT system, as seen from the inverter, is purely resistive, meaning that the voltage and current are perfectly in phase [12–14]. This eliminates reactive power and allows for maximum PTE. On the other hand, ZVS occurs when the current lags the voltage, which allows the inverter's switches to turn on and off with minimal power loss, thereby reducing switching losses and increasing overall PTE [15]. Therefore, the most efficient way to operate the system is by tuning it as close to the ZPA frequency as possible while still ensuring ZVS. This process involves operating in the inductive region, where soft switching is achievable, but still close enough to the ZPA to maintain a high PTE. Ultimately, ensuring that the system operates near ZPA is critical for optimizing the overall performance and efficiency of the WPT system.

Within the domain of WPT systems, two prominent topologies have garnered widespread attention: the series–series (S–S or SS) [16,17] and the double-sided inductor–capacitor–capacitor (LCC, LCC–LCC) topologies [18,19]. Among these, the SS topology is widely adopted in consumer electronics owing to its simplicity, ease of implementation, and effectiveness for short-range power transfer applications. This topology is particularly well-suited for devices such as smartphones, tablets, and other portable electronics, where compact designs, lower power levels, and efficient power transfer are critical. Its straightforward structure also minimizes the complexity of the system, making it ideal for mass-produced consumer devices.

Meanwhile, the double-sided LCC topology is primarily adopted in electric vehicles, which demand higher power and longer power transfer distances [18,19]. This topology offers advantages such as improved compensation, better voltage regulation, and more precise control over power flow, rendering it ideal for fulfilling the dynamic and high-power demands of electric vehicle charging systems. Additionally, the LCC topology provides robustness against misalignment, which is crucial in scenarios where precise coil alignment is challenging, such as in EVs. These distinct applications highlight not only the versatility of WPT technology but also the importance of selecting the correct topology to optimize efficiency, system stability, and performance based on the specific requirements of each target application. While recent studies, such as Corti et al. [20], have provided valuable optimization techniques for the SS topology, they do not address the double-sided LCC topology, which is key for high-power applications.

Although numerous studies have extensively explored techniques for realizing ZPA conditions in WPT systems [12–14], they often fail to address the critical issues of leakage magnetic fields. Specifically, studies related to ZPA realization in WPT systems lack efforts to mitigate leakage magnetic fields, which is crucial for ensuring both human safety and the commercial viability of the systems. While some methods, such as using shielding coils [21–23], have been proposed to suppress leakage magnetic fields, they introduce additional challenges, including increased spatial requirements and financial costs. Furthermore, attempts to modify topologies to address leakage issues often disregard the need to maintain ZPA conditions, which is crucial for optimizing PTE. In addition to these techniques, recent studies have shown that the spread spectrum technique, which involves modulating the inverter's switching frequency either periodically or randomly, can effectively reduce leakage magnetic fields and EMI without increasing spatial or financial burdens [24,25]. This approach provides a cost-effective alternative that can be implemented via software, addressing leakage magnetic fields while maintaining system efficiency. This oversight in existing research underscores the urgent need for novel approaches that can concurrently tackle ZPA and leakage magnetic field mitigation without affecting spatial or financial efficiency.

The key contribution of this study lies in the introduction of a novel method for selecting resonant circuit component values capable of simultaneously minimizing leakage magnetic fields and satisfying the ZPA condition in the two most widely used WPT topologies—the SS topology and the double-sided LCC topology. The proposed approach minimizes the phasor sum of the currents in the transmitter (TX) and receiver (RX) coils by

optimizing the RX-side resonant circuit. Meanwhile, the transmitter-side resonant circuit is designed to ensure that the impedance presented to the inverter satisfies the ZPA condition. This method has been mathematically derived and experimentally validated.

The remainder of this paper is structured as follows. In Section 2, the proposed method for selecting resonant circuit components that can achieve both leakage magnetic field suppression and the ZPA condition is mathematically derived and explained. Section 3 presents a validation of the proposed method based on simulated and experimental findings. Section 4 concludes the paper with a summary of the results. Additionally, Appendix A discusses the control loop for implementing the proposed system.

2. Method for Selecting a Resonant Capacitance That Minimizes Leakage Magnetic Fields While Satisfying the ZPA Condition

2.1. Factors Determining Leakage Magnetic Fields Within a WPT System

Before delving into the details of the proposed method, we first examine the factors influencing the leakage magnetic field generated by the coil. The magnetic field produced by a typical circular coil is represented by Equation (1) [26].

$$\vec{B} = \frac{\mu_0 N I r^2}{4d^2} sin\theta, \tag{1}$$

The components of Equation (1) are shown in Figure 1, where N represents the number of turns of the coil, r denotes the radius of the coil, d represents the distance from the center of the coil to the measurement point, and θ denotes the angle between the normal line to the plane of the coil and the line connecting the measurement point. As detailed in [26], under certain assumptions (e.g., $d \gg r$, and $N_{TX} = N_{RX}$), the magnitude of the leakage magnetic field produced by the coil can be expressed as indicated in Equation (2).

$$\left|\vec{B}\right| = \left|\vec{B_{TX}} + \vec{B_{RX}}\right| \propto |\mathbf{I_{TX}} + \mathbf{I_{RX}}| \tag{2}$$

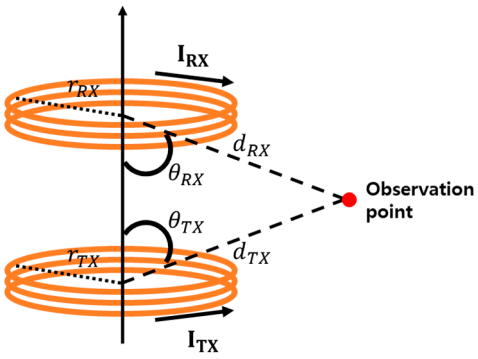

Figure 1. Leakage magnetic field at an arbitrary distance from the coil.

Thus, Equation (2) indicates that the magnitude of the leakage magnetic field generated by the operating WPT coil can be minimized by minimizing the vector phasor sum of the coil currents. Generally, when the resonant frequency on the RX side (ω_{RX}) is set to match the operating frequency of the inverter (ω_0), the currents flowing through the TX and RX coils exhibit a 90° phase difference, as illustrated in Figure 2a. In this scenario, only the magnitudes of the TX and RX coil currents can be adjusted. However, given that the currents flowing through most TX and RX coils are determined by the TX input voltage and the RX load, their adjustments are limited. However, as illustrated in Figure 2b,c, if the phase difference between the TX and RX currents, as well as their magnitudes, can be varied, the magnitude of the vector phasor sum of the currents—which determines the leakage magnetic field—can also change. The primary objective of this study is to identify the resonant condition that leads to the smallest current phasor sum.

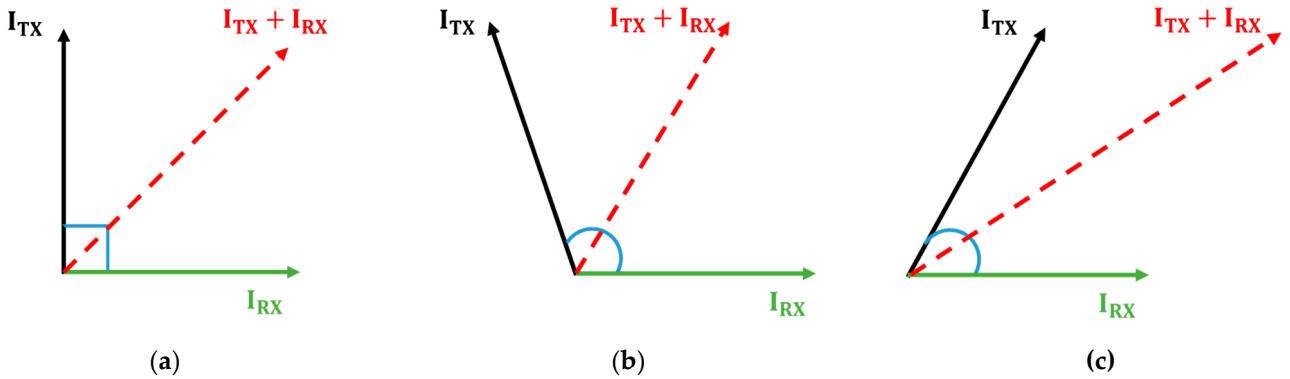

Figure 2. Phasor sum of the transmitter (TX) and receiver (RX) coil currents based on the phase difference. When the TX and RX coil currents exhibit (**a**) a 90° phase difference, (**b**) >90° phase difference, and (**c**) <90° phase difference.

2.2. Resonance Capacitance of a WPT System with SS Topology That Minimizes the Leakage Magnetic Field and Satisfies the ZPA Condition

Figure 3 depicts a WPT system featuring the SS topology. In this figure, from the inverter output to the rectifier input, only the fundamental component is expressed using phasor representation. This approach, known as the fundamental harmonic approximation, has been validated in numerous studies [27]. Furthermore, given that the value of the equivalent series resistance (ESR) is generally extremely small, it is assumed to be negligible. The relationship between the direct current (DC) input V_{in} applied to the WPT system and the root mean square value of the inverter output V_{inv} is expressed in Equation (3) [15], while the relationship between the equivalent load R_L observed from the rectifier input on the RX and the load resistance R_{load} is detailed in Equation (4) [15].

$$V_{inv} = \frac{4}{\pi\sqrt{2}} V_{in} \tag{3}$$

$$R_L = \frac{8}{\pi^2} R_{load} \tag{4}$$

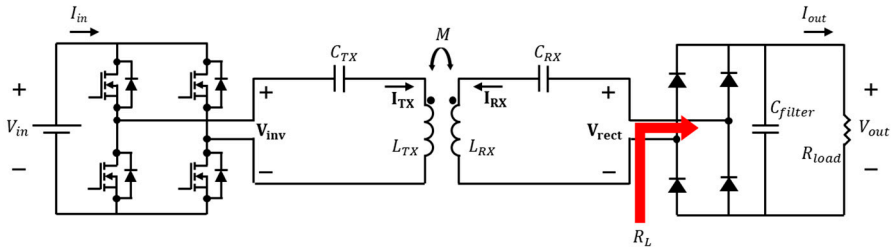

Figure 3. Wireless power transfer (WPT) system featuring the series–series (SS) topology.

Applying Kirchhoff's voltage law (KVL, loop equation) using only the alternating current (AC) components in the circuit depicted in Figure 3 results in Equations (5) and (6).

$$\mathbf{V_{inv}} = \left(\frac{1}{j\omega_o C_{TX}} + j\omega_o L_{TX}\right)\mathbf{I_{TX}} + j\omega_o M\mathbf{I_{RX}} \tag{5}$$

$$-j\omega_o M\mathbf{I_{TX}} = \left(j\omega_o L_{RX} + \frac{1}{j\omega_o C_{RX}} + R_L\right)\mathbf{I_{RX}} \tag{6}$$

where ω_o denotes the operating frequency of the WPT system. By calculating the ratio of the TX coil current ($\mathbf{I_{TX}}$) to the RX coil current ($\mathbf{I_{RX}}$) using Equation (6), we obtain Equation (7).

$$\frac{\mathbf{I_{TX}}}{\mathbf{I_{RX}}} = \frac{\sqrt{R_L^2 + X_{RX}^2}}{\omega_o M} \angle (\arctan(\frac{X_{RX}}{R_L}) + \frac{\pi}{2}), \tag{7}$$

where X_{RX} represents the reactance caused by the coil and capacitance on the RX side ($X_{RX2} = \omega_o L_{RX} - 1/\omega_o C_{RX}$). To identify the condition that minimizes the leakage magnetic field while maintaining the same output ($I_{RX}^2 R_L$) for a given load, the magnitude of the RX current (I_{RX}) is fixed, and its phase is set as the reference (i.e., 0 rad or°), as indicated in Equation (8). Notably, we fix the magnitude of I_{RX} because the proposed scheme is later compared with control methods under the same condition.

$$\mathbf{I_{RX}} = I_{RX} \angle 0^\circ \tag{8}$$

Using Equations (7) and (8), the TX current ($\mathbf{I_{TX}}$) can be expressed as indicated in Equation (9).

$$\mathbf{I_{TX}} = \frac{I_{RX}\sqrt{R_L^2 + X_{RX}^2}}{\omega_o M} \angle (\arctan(\frac{X_{RX}}{R_L}) + \frac{\pi}{2}) \tag{9}$$

Equation (9) indicates that the phase difference between $\mathbf{I_{TX}}$ and $\mathbf{I_{RX}}$ depends on the value of X_{RX}. If X_{RX} is negative, the phase difference is acute; if X_{RX} is zero, the phase difference is 90°; and if X_{RX} is positive, the phase difference is obtuse. These phase differences are illustrated in Figure 2.

According to Equation (2), to minimize the leakage magnetic field in the WPT system, the magnitude of the vector phasor sum of the TX and RX currents must be minimized. To identify the corresponding resonance condition, an analysis based on Figure 4 is conducted. In Figure 4, l denotes the magnitude of the sum of the TX and RX currents, which is to be minimized. This parameter l can be expressed using the law of cosines, as detailed in Equation (10).

$$\begin{aligned} l^2 &= |\mathbf{I_{TX}}|^2 + |\mathbf{I_{RX}}|^2 - 2|\mathbf{I_{TX}}||\mathbf{I_{RX}}|\cos\theta \\ &= I_{RX}^2 \left(\frac{R_L^2 + X_{RX}^2 + \omega_o^2 M^2 - 2X_{RX}\omega_o M}{\omega_o^2 M^2} \right) = I_{RX}^2 f(X_{RX}) \end{aligned} \tag{10}$$

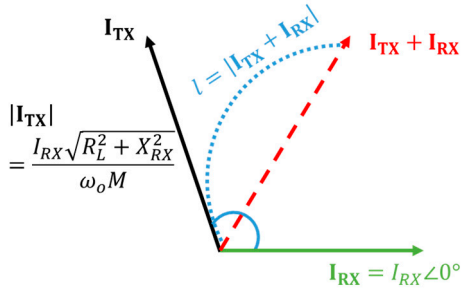

Figure 4. TX and RX current phasor diagram according to the resonance condition in the SS topology.

In Equation (10), $f(X_{RX})$ is a function with reactance X_{RX} as the variable. To determine the value of the RX-side reactance that minimizes the magnitude of the sum of the TX and RX currents, we differentiate $f(X_{RX})$, yielding Equation (11). The condition for X_{RX} that makes Equation (11) equal to zero is presented in Equation (12).

$$\frac{\partial f(X_{RX})}{\partial X_{RX}} = \frac{2(\mathrm{X_{RX}} - \omega_o M)}{{\omega_o}^2 M^2} \tag{11}$$

$$X_{RX} = \omega_o M \tag{12}$$

Given that the inductance L_{TX} of the RX coil is fixed, the resonance capacitance value C_{RX} that satisfies Equation (12) is as detailed in Equation (13).

$$C_{RX} = \frac{1}{\omega_o^2(L_{RX} - M)} \tag{13}$$

Additionally, the resonance frequency ω_{RX} on the RX side is detailed in Equation (14), and the sum of the TX and RX currents when (14) is chosen as the resonant frequency on the RX side is given by Equation (15).

$$\omega_{RX} = \omega_o \sqrt{\frac{L_{RX} - M}{L_{RX}}} \tag{14}$$

$$\mathbf{I_{total}} = \mathbf{I_{TX}} + \mathbf{I_{RX}} = I_{RX}\left(\frac{\sqrt{R_L^2 + (\omega_o M)^2}}{\omega_o M} \angle\left(arctan\left(\frac{\omega_o M}{R_L}\right) + \frac{\pi}{2}\right) + 1\right) \tag{15}$$

The sum of the currents in Equation (15) is proportional to the leakage magnetic field in the WPT system, as analyzed in Equation (2). In other words, since the magnitude of the sum of the TX and RX currents has reached its minimum ($|\mathbf{I_{TX}} + \mathbf{I_{RX}}|$), the leakage magnetic field will also be minimized. Thus, we have obtained the RX resonance capacitance (C_{RX}) that minimizes the leakage magnetic field in the WPT system with the SS topology, as detailed in Equation (13). This capacitance is independent of the resonance frequency on the TX side and depends exclusively on the resonance value on the RX side.

Using Equations (9) and (12), the required magnitude of TX current to transfer the same power to the load in both the conventional and proposed systems can be determined. For the conventional system, this corresponds to the cases where $X_{RX} = 0$ in Equation (9), and the magnitude of $\mathbf{I_{TX}}$ can be expressed as in (16).

$$|\mathbf{I_{TX,conv}}| = \frac{I_{RX}\sqrt{R_L^2}}{\omega_o M} \tag{16}$$

Similarly, for the proposed system, where $X_{RX} = \omega_o M$ in Equation (9), the magnitude of $\mathbf{I_{TX}}$ can be expressed as in (17).

$$|\mathbf{I_{TX,prop}}| = \frac{I_{RX}\sqrt{R_L^2 + (\omega_o M)^2}}{\omega_o M} \tag{17}$$

Although Equation (13) provides a condition that guarantees the minimization of the leakage magnetic field within a WPT system featuring an SS topology, it does not ensure a purely resistive input impedance on the TX-side inverter. Specifically, tuning the resonance according to Equation (13) fails to satisfy the ZPA condition, as the RX resonance frequency, ω_{RX}, differs from the system's operating frequency, ω_o. To address this, we will now derive the resonance condition on the TX side that satisfies the ZPA condition for the system. By substituting the result derived from Equation (12) into Equation (6) and expressing the ratio of $\mathbf{I_{RX}}$ to $\mathbf{I_{TX}}$, we obtain the expression detailed in Equation (18).

$$\frac{\mathbf{I_{RX}}}{\mathbf{I_{TX}}} = \frac{-j\omega_o M}{j\omega_o M + R_L} \tag{18}$$

Meanwhile, the input impedance, Z_{in}, of the WPT system as seen from the inverter can be calculated by dividing both sides of Equation (5) by $\mathbf{I_{TX}}$. By expressing $\mathbf{I_{RX}}$ in terms of $\mathbf{I_{TX}}$ using Equation (18), dividing the inverter output voltage ($\mathbf{V_{inv}}$) by the inverter output

current ($\mathbf{I_{TX}}$), which defines the input impedance ($Z_{in} = \mathbf{V_{inv}}/\mathbf{I_{TX}}$), and simplifying the resulting expression, we obtain Equation (19).

$$Z_{in} = \frac{\omega_o^2 M^2 R_L}{R_L^2 + \omega_o^2 M^2} + j(\omega_o L_{TX} - \frac{1}{\omega_o C_{TX}} - \frac{\omega_o^3 M^3}{R_L^2 + \omega_o^2 M^2}) \quad (19)$$

To satisfy the ZPA condition, the imaginary part of the input impedance, Z_{in}, must be zero. This implies that the imaginary part of Equation (19) must be zero. The TX-side resonance capacitance, C_{TX}, that satisfies this condition is expressed in Equation (20).

$$C_{TX} = \frac{1}{\omega_o^2 (L_{TX} - \frac{\omega_o^2 M^3}{R_L^2 + \omega_o^2 M^2})} \quad (20)$$

Table 1 presents the proposed TX and RX resonance capacitance values and required magnitude of target TX current for a WPT system with an SS topology. These values minimize the leakage magnetic field while satisfying the ZPA condition and transfer same output power to the load.

Table 1. Proposed TX and RX resonance capacitances that minimize the leakage magnetic field while satisfying the ZPA condition and required magnitude of TX current to transfer the same power to the load for an SS topology.

Parameters	Conventional Value	Proposed Value	Role
C_{TX}	$\frac{1}{\omega_o^2 L_{TX}}$	$\frac{1}{\omega_o^2 \left(L_{TX} - \frac{\omega_o^2 M^3}{R_L^2 + \omega_o^2 M^2} \right)}$	Satisfaction of the ZPA Condition
C_{RX}	$\frac{1}{\omega_o^2 L_{RX}}$	$\frac{1}{\omega_o^2 (L_{RX} - M)}$	Minimization of Leakage Magnetic Field
$\lvert \mathbf{I_{TX}} \rvert$	$\frac{I_{RX}\sqrt{R_L^2}}{\omega_o M}$	$\frac{I_{RX}\sqrt{R_L^2 + (\omega_o M)^2}}{\omega_o M}$	Required Magnitude of Target Current to Transfer Same Power to Load

2.3. Resonance Capacitance of a WPT System with Double-Sided LCC Topology That Minimizes the Leakage Magnetic Field and Satisfies the ZPA Condition

Figure 5 presents the circuit diagram of a WPT system featuring the double-sided LCC topology. Similar to the SS topology, the condition for minimizing the leakage magnetic field in the double-sided LCC topology depends on the values of the components on the RX side. To analyze these component values, the AC equivalent circuit of the RX side is illustrated in Figure 6.

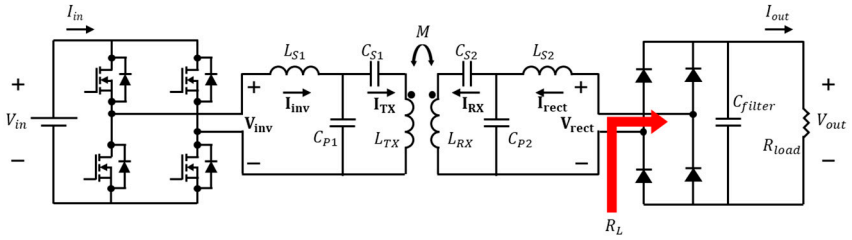

Figure 5. WPT system featuring the double-sided inductor–capacitor–capacitor (LCC) topology.

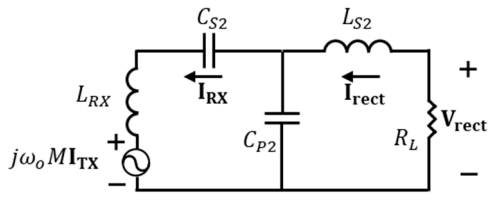

Figure 6. RX-side AC equivalent circuit of the WPT system depicted in Figure 5.

Applying KVL to the circuit depicted in Figure 6 yields Equations (21) and (22).

$$-j\omega_o M\mathbf{I_{TX}} = j\left(\omega_o L_{RX} - \frac{1}{\omega_o C_{S2}} - \frac{1}{\omega_o C_{P2}}\right)\mathbf{I_{RX}} - \frac{1}{j\omega_o C_{P2}}\mathbf{I_{rect}} \tag{21}$$

$$\left(j\omega_o L_{S2} + \frac{1}{j\omega_o C_{P2}} + R_L\right)\mathbf{I_{rect}} - \frac{1}{j\omega_o C_{P2}}\mathbf{I_{RX}} = 0 \tag{22}$$

If the resonance frequency of L_{S2} and C_{P2} is set equal to the operating frequency, we obtain Equation (23). Substituting this equation into Equation (22) yields Equation (24). Additionally, substituting Equation (24) into Equation (21) yields the ratio of $\mathbf{I_{TX}}$ to $\mathbf{I_{RX}}$, as indicated in Equation (25).

$$\omega_o L_{S2} - \frac{1}{\omega_o C_{P2}} = 0 \tag{23}$$

$$\mathbf{I_{rect}} = \frac{1}{j\omega_o C_{P2} R_L}\mathbf{I_{Rx}} \tag{24}$$

$$\frac{\mathbf{I_{TX}}}{\mathbf{I_{RX}}} = \frac{\sqrt{\alpha^2+\beta^2}}{\omega_o M}\angle\left(\frac{\pi}{2} + \arctan\left(\frac{\beta}{\alpha}\right)\right) \tag{25}$$

In Equation (25), α and β are defined as presented in Equations (26) and (27).

$$\alpha = \frac{1}{\omega_o^2 C_P^2 R_L} \tag{26}$$

$$\beta = \omega_o(L_{RX} - L_{S2}) - \frac{1}{\omega_o C_{S2}} \tag{27}$$

If $\mathbf{I_{RX}}$ is considered as the phasor reference ($\mathbf{I_{RX}} = I_{RX}\angle 0°$), $\mathbf{I_{TX}}$ can be expressed as presented in Equation (28) based on Equation (25).

$$\mathbf{I_{TX}} = \frac{I_{RX}\sqrt{\alpha^2+\beta^2}}{\omega_o M}\angle\left(\frac{\pi}{2} + \arctan\left(\frac{\beta}{\alpha}\right)\right) \tag{28}$$

The phasor diagram for the sum of the currents, as depicted in Figure 7, is redrawn based on Equation (28). To minimize the leakage magnetic field, the magnitude of the sum of $\mathbf{I_{TX}}$ and $\mathbf{I_{RX}}$, denoted as l, must be minimized. The squared magnitude of this sum is expressed in Equation (29).

$$l^2 = I_{RX}^2\left(\frac{\alpha^2+\beta^2+\omega_o^2M^2-2\beta\omega_o M}{\omega_o^2 M^2}\right) = I_{RX}^2 g(\beta) \tag{29}$$

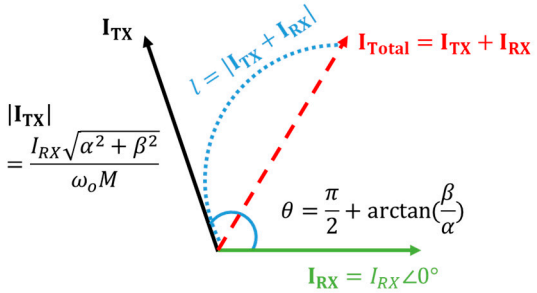

Figure 7. TX and RX current phasor diagram based on the resonance condition of the double-sided LCC topology.

To determine the minimum value of l, the function $g(\beta)$ in Equation (29) is differentiated, yielding Equation (30). The value of β that satisfies the minimum condition is detailed in Equation (31).

$$\frac{\partial g(\beta)}{\partial \beta} = \frac{2(\beta - \omega_o M)}{{\omega_o}^2 M^2} \tag{30}$$

$$\beta = \omega_o L_{RX} - \omega_o L_{S2} - \frac{1}{\omega_o C_{S2}} = \omega_o M \tag{31}$$

Finally, by rearranging Equation (31), the resonant capacitance C_{S2} that minimizes the leakage magnetic field in the double-sided LCC topology can be derived, as detailed in Equation (32). Additionally, when the capacitance value in Equation (30) is selected as the value of C_{S2} on the RX side, the sum of the TX and RX currents is given by Equation (33).

$$C_{S2} = \frac{1}{\omega_o^2 (L_{RX} - L_{S2} - M)} \tag{32}$$

$$\mathbf{I_{total}} = \mathbf{I_{TX}} + \mathbf{I_{RX}} = I_{RX}\left(\frac{\sqrt{\alpha^2 + \omega_o M^2}}{\omega_o M} \angle \left(arctan\left(\frac{\omega_o M}{\alpha}\right) + \frac{\pi}{2}\right) + 1\right) \tag{33}$$

Equation (33) shows the minimum value of the phasor sum of the TX and RX currents under the given conditions. Therefore, as indicated by Equation (2), when the phasor sum of the currents is minimized, the leakage magnetic field is also minimized. Thus, in a WPT system with the double-sided LCC topology, selecting C_{S2} according to Equation (32) minimizes the leakage magnetic field.

Using a method like the SS topology, and with Equations (28) and (31), the required magnitude of TX current to transfer the same power to the load in both the conventional and proposed systems can be determined. For the conventional system, this corresponds to the cases where $\beta = 0$ in Equation (28), and the magnitude of $\mathbf{I_{TX}}$ can be expressed as in (34).

$$|\mathbf{I_{TX,conv}}| = \frac{I_{RX}\sqrt{\alpha^2}}{\omega_o M} \tag{34}$$

Similarly, for the proposed system, where $\beta = \omega_o M$ in Equation (26), the magnitude of $\mathbf{I_{TX}}$ can be expressed as in (35).

$$|\mathbf{I_{TX,prop}}| = \frac{I_{RX}\sqrt{\alpha^2 + (\omega_o M)^2}}{\omega_o M} \tag{35}$$

Equation (36) presents the general equation for the WPT system with a double-sided LCC topology. To obtain the value of $\mathbf{I_{inv}}$, the RX-side resonance conditions of L_{S2} and C_{P2}, as detailed in Equation (23), the value of C_{S2}, as determined by Equation (32) for minimizing the leakage magnetic field, and the resonance conditions of L_{S1} and C_{P1} on the TX side of the double-sided LCC topology in Equation (37) are substituted into Equation (36), yielding Equation (38).

$$\begin{bmatrix} j\omega_o L_{S1} + \frac{1}{j\omega_o C_{P1}} & \frac{-1}{j\omega_o C_{P1}} & 0 & 0 \\ \frac{-1}{j\omega_o C_{P1}} & \frac{1}{j\omega_o C_{P1}} + \frac{1}{j\omega_o C_{S1}} + j\omega_o L_{TX} & j\omega_o M & 0 \\ 0 & j\omega_o M & \frac{1}{j\omega_o C_{P2}} + \frac{1}{j\omega_o C_{S2}} + j\omega_o L_{RX} & \frac{-1}{j\omega_o C_{P2}} \\ 0 & 0 & \frac{-1}{j\omega_o C_{P2}} & j\omega_o L_{S2} + \frac{1}{j\omega_o C_{P2}} + R_L \end{bmatrix} \begin{bmatrix} \mathbf{I_{inv}} \\ \mathbf{I_{TX}} \\ \mathbf{I_{RX}} \\ \mathbf{I_{rect}} \end{bmatrix} = \begin{bmatrix} \mathbf{V_{inv}} \\ 0 \\ 0 \\ 0 \end{bmatrix} \tag{36}$$

$$\omega_o L_{S1} - \frac{1}{\omega_o C_{P1}} = 0 \tag{37}$$

$$\mathbf{I_{inv}} = \frac{\left(MR_L + C_{S1}M^2R_L\omega_o^2 + \sigma_2 - C_{S1}L_{TX}MR_L\omega_o^2 - jL_{S2}^2\omega_o - \sigma_1 + jC_{S1}L_{S2}^2L_{TX}\omega_o^3\right)}{jL_{S1}\omega_o(-\sigma_2 + \sigma_1)}\mathbf{V_{inv}} \tag{38}$$

In Equation (38), σ_1 and σ_2 are introduced for calculation convenience and are defined as in Equations (39) and (40), respectively.

$$\sigma_1 = jC_{S1}L_{S1}LS_2^2\omega_o^2 \tag{39}$$

$$\sigma_2 = C_{S1}L_{S1}MR_L\omega_o^2 \tag{40}$$

Using Equation (38), the input impedance (Z_{in}) observed from the inverter can be determined. Similar to the SS topology, the input impedance (Z_{in}) in the double-sided LCC topology denotes the ratio of the inverter output voltage to the inverter output current $(Z_{in} = \mathbf{V_{inv}}/\mathbf{I_{inv}})$. To satisfy the ZPA condition in the WPT system, the phase difference between the inverter's output voltage $(\mathbf{V_{inv}})$ and current must be zero $(\mathbf{I_{inv}})$. To achieve this using Z_{in}, the imaginary part of the input impedance (Z_{in}) must be zero. The TX-side series capacitance (C_{S1}) that satisfies this condition is detailed in Equation (41).

$$C_{S1} = \frac{1}{\omega_o^2\left\{L_{TX} - L_{S1}\left(1 + \frac{M^3R_L^2}{L_{S1}\left(L_{S2}^4\omega_o^2 + M^2R_L^2\right)}\right)\right\}} \tag{41}$$

Table 2 compares the conventional resonant capacitance values with the proposed values (C_{S1} and C_{S2}) for minimizing the leakage magnetic field while satisfying the ZPA condition, as well as the required magnitude of TX current to transfer the same output power to the load in the double-sided LCC topology. Notably, the resonances between L_{S1} and C_{P2} and between L_{S2} and C_{P2} are detailed in Equations (37) and (23), respectively. These are identical to those corresponding to the conventional double-sided LCC topology [18,19].

Table 2. Proposed TX and RX resonance capacitances that minimize the leakage magnetic field while satisfying the ZPA condition and required magnitude of TX current to transfer the same power to the load for the double-sided LCC topology.

Parameters	Conventional Value	Proposed Value	Role
C_{S1}	$\frac{1}{\omega_o^2(L_{TX}-L_{S1})}$	(41)	Satisfaction of the ZPA Condition
C_{S2}	$\frac{1}{\omega_o^2(L_{RX}-L_{S2})}$	(32)	Minimization of Leakage Magnetic Field
$\lvert\mathbf{I_{TX}}\rvert$	$\frac{I_{RX}\sqrt{\alpha^2}}{\omega_o M}$	$\frac{I_{RX}\sqrt{\alpha^2+(\omega_o M)^2}}{\omega_o M}$	Required Magnitude of Target Current to Transfer Same Power to Load

As seen in Tables 1 and 2, the proposed method minimizes the magnetic field while satisfying the ZPA condition for both SS and LCC–LCC topologies. By identifying the conditions that satisfy ZPA and adjusting the TX resonant capacitor, the proposed method can also achieve ZVS, allowing it to maintain a power electronics circuit with a high efficiency. However, because the required target current of the TX coil to transfer the same power to the load is larger in the proposed system than in the conventional system, the coil-to-coil efficiency decreases, which may lead to a reduction in the overall system efficiency. While the existing reactive [21] or active shielding [23] methods also increase the TX coil current to transfer the same power, the proposed method has significant spatial advantages since it does not require additional shielding coils.

3. Verification

3.1. Verification Through Simulation

Figure 8 illustrates the coil set designed for the validation of the proposed system simulation. This figure also includes the geometrical dimensions of the coil set, while

additional simulation setup details are presented in Table 3. To minimize the leakage magnetic field of the coil, ferrite with a high permeability is added, and an aluminum case (housing) is included to simulate the actual wireless charging system. The coil system is analyzed using ANSYS Maxwell (version: 2024R1), which is a finite-element-method-based magnetic field analysis software.

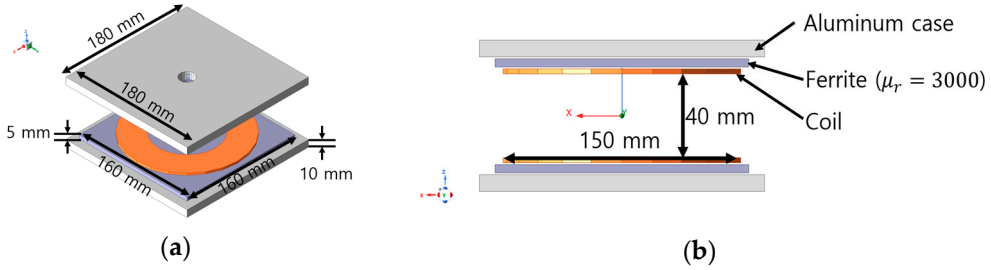

Figure 8. WPT coil set for simulation validation: (**a**) bird's-eye view and (**b**) cross-sectional view.

Table 3. Details regarding the simulation environment and coil wire material.

Parameters	Value
Operating frequency	85 kHz
Air gap	40 mm
Diameter of coil wire	2.8 mm
Number of turns of coils	12 turns

Table 4 presents the inductance and mutual inductance values derived from the magnetic field analysis simulation, along with the target output power for the power transfer simulation performed using a circuit simulator and the corresponding resistance values. As indicated in Table 4, the target output power is set to 100 W. This means that regardless of the input and output conditions, the output power for each resonant system is constant, while the input voltage is adjusted to ensure that the output reaches 100 W. The circuit simulation is configured using the equivalent circuit depicted in Figure 3. Notably, the parameter abbreviations in Table 4 correspond to the circuit components in Figure 3.

Table 4. Inductance values derived from the simulation, along with the target output power and equivalent load values used in the circuit simulation.

Parameters	Value
Inductance of the TX and RX coils (L_{TX}, L_{RX})	36.5 μH
Mutual inductance between the TX and RX coils (M)	13 μH
Target output power	100 W
Load resistance (R)	8.56 Ω

The circuit simulation confirms that when the resonant system is configured using the proposed method, the phasor sum of the current is minimized. Specifically, as indicated in Equation (13), when the resonance capacitor on the RX side is configured according to the proposed method, the phasor vector sum of the current, depicted in Figure 4, is minimized. Table 5 lists the resonant capacitance values and resonant frequency values on the RX side used in the simulation. In this table, the "Conventional" values correspond to the RX resonant frequencies that are precisely matched with the operating frequency, as proposed in previous studies and detailed in Table 1. Meanwhile, the "Proposed" values represent the resonant settings determined by the method proposed in this study. The remaining two cases represent additional comparison groups that are set for further evaluation.

Table 5. RX-side resonant capacitance values and the resonant frequency used in the circuit simulation.

Parameters	C_{RX}	RX Resonant Frequency
Conventional	100 nF	84.12 kHz
Proposed	159 nF	66.71 kHz
Comparison group 1	120 nF	76.8 kHz
Comparison group 2	70 nF	100 kHz

Table 6 illustrates the TX and RX coil currents and the corresponding phase differences based on changes in the RX resonant capacitance values detailed in Table 5. The "Conventional" values demonstrate a phase difference of nearly 90° between the TX and RX currents, while the proposed method achieves a phase difference of 142.3°.

Table 6. Currents and phase differences between the TX and RX currents based on changes in RX resonant capacitance values.

Parameters	$\|I_{TX}\|$ [A]	$\|I_{RX}\|$ [A]	Phase Difference [°]
Conventional	5.90	5.54	96.5
Proposed	8.37	5.39	142.3
Comparison group 1	6.53	5.43	119.6
Comparison group 2	7.93	5.36	46.4

The vector phasor sums of the TX and RX currents, calculated based on the phase differences, are illustrated in Figure 9. As depicted in Figure 9, when the RX resonant capacitance is determined using the proposed method, the vector phasor sum of the TX and RX currents is minimized. This aligns with our previous inference that minimizing the vector phasor sum of the TX and RX currents will also minimize the radiated leakage magnetic field, as indicated in Equation (2). While the simulation only confirms the minimization of the vector phasor sum of the TX and RX currents using the proposed method, subsequent experiments validate the minimization of the magnetic field as well, confirming this inference.

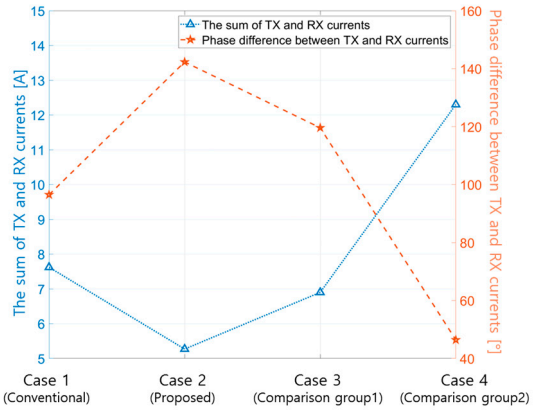

Figure 9. Effects of RX resonant capacitance on the magnitudes and phase differences of TX and RX currents in a WPT with the SS topology.

The results summarized in Table 7 confirm the effectiveness of the TX resonant capacitance values proposed in this paper to satisfy the ZPA condition. Specifically, when resonance is set according to the values specified in Table 5, the reactance on the RX side is not completely eliminated. Consequently, from the perspective of the inverter output, the WPT system fails to achieve proper resonance and satisfy the ZPA condition. This can be observed in the "Conventional" section of Table 7, where the TX resonant capacitance

is set to conventional values (refer to Table 1). In this case, the phase difference between the inverter output voltage and current reaches 49°. Conversely, when the TX resonant capacitance is selected based on Equation (20), the power factor substantially increases from 0.655 to 0.971. Additionally, the phase difference between the inverter output voltage and current decreases from 49° to 14°. These findings demonstrate that selecting the TX and RX resonant capacitances as proposed in this study minimizes the sum of the TX and RX coil currents, which reduces the leakage magnetic field of the WPT system and helps satisfy the ZPA condition.

Table 7. Inverter output voltages and current power factors, along with phase differences, based on TX resonant capacitances.

Parameters	C_{TX}	Power Factor	Phase Difference [°]
Conventional	100 nF	0.655	49
Proposed	120 nF	0.971	14

To further validate the effectiveness of the proposed resonant values in minimizing the leakage magnetic field and satisfying the ZPA condition for the double-sided LCC topology, a simulation is conducted using the circuit diagram depicted in Figure 5. Table 8 illustrates the series inductance (L_{S1} and L_{S2}) and parallel capacitance values (C_{P1} and C_{P2}) for the double-sided LCC topology.

Table 8. Resonant component values for the double-sided LCC topology (L_{S1}, L_{S2}, C_{P1}, and C_{P2}).

Parameters	Value
Series inductance (L_{S1} and L_{S2})	12.4 μH
Parallel capacitance (C_{P1} and C_{P2})	282 nF

Table 9 lists the RX series capacitance values used in the circuit simulation. Similar to the SS topology, two scenarios are also established in the double-sided LCC topology: "Conventional", where the resonant capacitance is set according to existing studies, and "Proposed", where the resonant capacitance is set according to the method proposed in this paper. The specific formulas for setting these resonant values are detailed in Table 2, and the proposed relation for determining the RX series capacitance is detailed in Equation (32). Two additional comparison groups are established for further evaluation (Comparison groups 1 and 2). Table 9 specifies the resonant frequency for each case.

Table 9. RX series capacitance values and resonant frequency used in the circuit simulation.

Parameters	C_{S2}	Resonance Frequency ($\frac{1}{2\pi\sqrt{(L_{RX}-L_{S2})\times C_{S2}}}$)
Conventional	141 nF	87.7 kHz
Proposed	328 nF	57.8 kHz
Comparison group 1	120 nF	95.0 kHz
Comparison group 2	100 nF	104 kHz

Table 10 summarizes the magnitudes and phase differences of the TX and RX currents as functions of the RX series capacitance values. Figure 10 visually depicts the vector phasor sum of these currents, derived from the data presented in Table 10. Similar to the SS topology, for the double-sided LCC topology, when the RX series capacitance is determined using the method proposed in this paper, the vector phasor sum of the TX and RX currents reaches its minimum value. This demonstrates the effectiveness of the proposed approach in decreasing the value of the overall current phasor sum, which is critical for minimizing the leakage magnetic field.

Table 10. Currents and phase differences between the TX and RX currents based on changes in the RX series capacitance.

Parameters	$\|I_{TX}\|$ [A]	$\|I_{RX}\|$ [A]	Phase Difference [°]
Conventional	5.69	6.28	67.3
Proposed	6.84	6.14	131.8
Comparison Group 1	6.19	5.93	123.4
Comparison Group 2	8.70	6.18	36.4

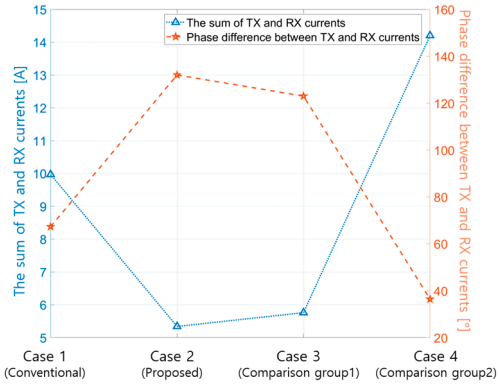

Figure 10. Effects of RX resonant capacitance on the magnitude and phase difference of the TX and RX currents in a WPT system with the double-sided LCC topology.

Finally, the results summarized in Table 11 demonstrate the effectiveness of the proposed method in providing the TX-side series inductance value that satisfies the ZPA condition. In the "Conventional" case, where the resonant capacitance is selected according to previous methods, tuning the capacitance makes the reactance on the RX side equal to zero, ensuring that the ZPA condition is satisfied. However, when the RX series capacitance is adjusted using the method proposed in this paper, the reactance is not completely eliminated, leading to a non-zero imaginary part of the impedance, as observed from the inverter. Consequently, the ZPA condition is not fully satisfied. To resolve this issue, by adjusting the TX series capacitance using the proposed Equation (41), the reactance of the WPT system seen from the inverter can be eliminated, thereby satisfying the ZPA condition. This solution increases the power factor from 0.644 to 0.960 and reduces the phase difference from 49° to 16°.

Table 11. Inverter output voltages and current power factors, along with phase differences, under varying TX series capacitances (C_{S1}).

Parameters	C_{S1}	Power Factor	Phase Difference [°]
Conventional	141 nF	0.644	49
Proposed	206 nF	0.960	16

3.2. Verification Through Experiments

Figure 11 illustrates the experimental setup for validating the proposed method. Notably, to ensure accurate testing, input power is supplied via a DC power supply (V_{in}), as illustrated in Figure 11a, while AC power is delivered to the WPT coils and resonance circuit through an inverter (V_{inv}). On the RX side, the power reaches the DC load through the RX resonance circuit and rectifier. All time-domain waveforms are captured using an oscilloscope, while the magnetic field is quantified using a magnetic field meter. Furthermore, as presented in Figure 11b, the coil system used in the simulation is practically fabricated for the experiment. Similar to the simulation model, the practical coil comprises ferrite, aluminum, and coils. Furthermore, the type and number of turns are identical to those used in the simulation, as detailed in Table 3. Table 12 presents the electrical

parameters of the fabricated coils, which are illustrated in Figure 11b, and the target output power values used in the experiment.

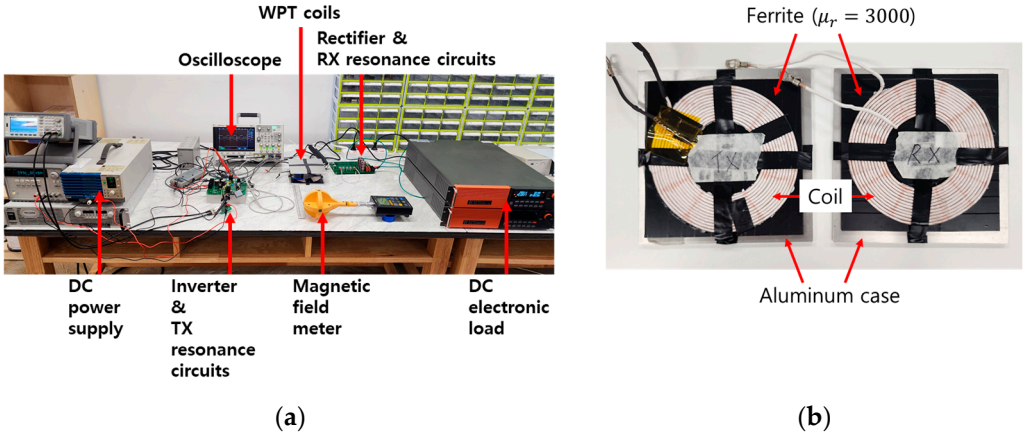

Figure 11. Experimental setup for WPT validation: (**a**) overall configuration and (**b**) WPT coil set.

Table 12. Electrical parameters of the fabricated WPT coil set, target output power, and output load used in the experiment.

Parameters	Value
Inductance of the TX and RX coils (L_{TX}, L_{RX})	35.8 µH
ESR of the coils	50 mΩ
Mutual inductance between the TX and RX coils (M)	12.6 µH
Target output power	100 W
Load resistance (R)	8.56 Ω

Table 13 lists the resonance capacitances used to verify the effectiveness of the proposed method in a WPT system with the SS topology. Unlike the simulation, in the experiment, the TX capacitance for satisfying the ZPA condition and the RX capacitance for minimizing the leakage magnetic field are applied simultaneously. Specifically, the experimental group uses the proposed method and the control group employs the conventional resonance method. The selection of TX and RX resonant capacitances, as outlined in Table 13, is based on the equations detailed in Table 1.

Table 13. Resonant capacitors used in the experiment of the WPT system with the SS topology.

Parameters	SS Conventional	SS Proposed
C_{TX}	100 nF	100 nF
C_{RX}	120 nF	159 nF

Figure 12 and Table 14 compare the magnitudes and phase differences of the TX and RX currents when using the conventional and proposed methods for selecting the resonance capacitance in the SS topology. As indicated in Table 14, similar to the simulation results, the proposed method reduces the magnitude of the current phasor sum from 9.10 to 7.31 A, demonstrating an approximately 20% reduction compared to the conventional method. This decrease in the current phasor sum suggests a corresponding reduction in the leakage magnetic field when using the proposed method.

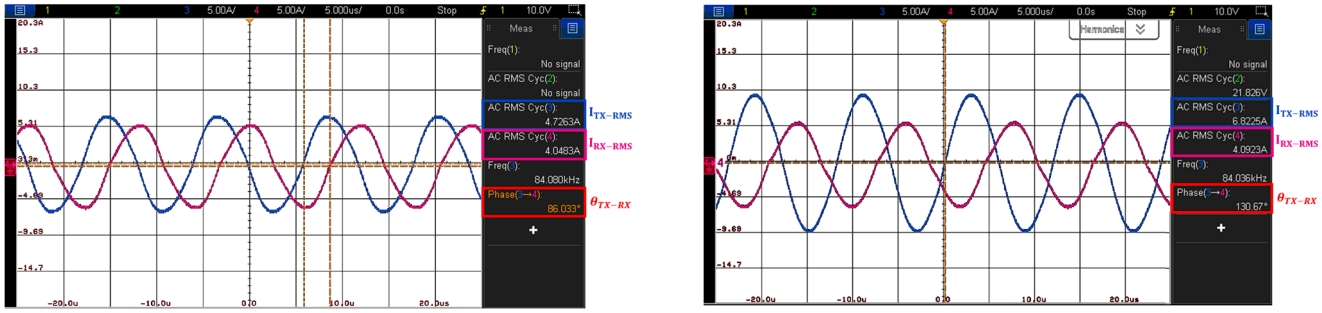

(**a**) (**b**)

Figure 12. Current magnitudes and phase changes as functions of the resonance capacitance in the WPT system with the SS topology: (**a**) when resonance capacitances are set based on conventional methods and (**b**) the proposed method.

Table 14. Magnitudes and phase differences of the current vector sum for the conventional and proposed resonance capacitance determination methods in the WPT system with the double-sided SS topology.

Parameters	S–S Conventional	S–S Proposed
$\lvert\mathbf{I_{TX}} + \mathbf{I_{RX}}\rvert$	9.10 A	7.31 A
Phase difference between $\mathbf{I_{TX}}$ and $\mathbf{I_{RX}}$	86°	131°

Figure 13 presents the measured magnetic field as a function of the distance from the WPT coil, which is depicted in Figure 11a. As depicted, the magnetic field is measured at five different distances from the side of the coil, ranging from 100 to 300 mm, using a magnetic field meter antenna. As illustrated in Figure 13, the proposed method consistently results in lower measured magnetic fields compared to those resulting from the conventional method, regardless of the distance. Specifically, the proposed method reduces the magnetic field by varying extents, from 7% to 35%, depending on the distance. This demonstrates the effectiveness of the proposed method in reducing leakage magnetic fields.

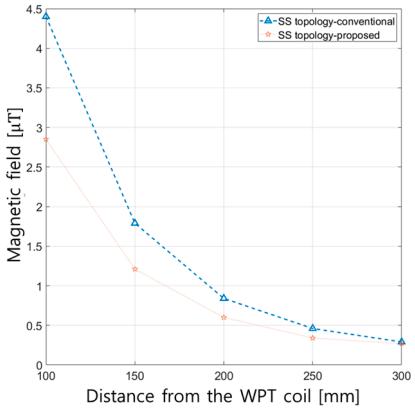

Figure 13. Magnetic field as a function of the distance from the WPT foil when applying the proposed and conventional methods to the WPT system with the SS topology.

Finally, Figure 14 illustrates the variations in the ZPA characteristics of the WPT system with the SS topology depending on the method used to determine the resonant capacitance. Similar to the previous simulations, this test also confirms that selecting the resonant capacitance using the proposed method improves the ZPA performance compared to the conventional method. Specifically, when using the conventional method, the phase difference between the output voltage and current of the inverter is 20.9°. Conversely, when using the proposed method, this phase difference is reduced to 4.8°.

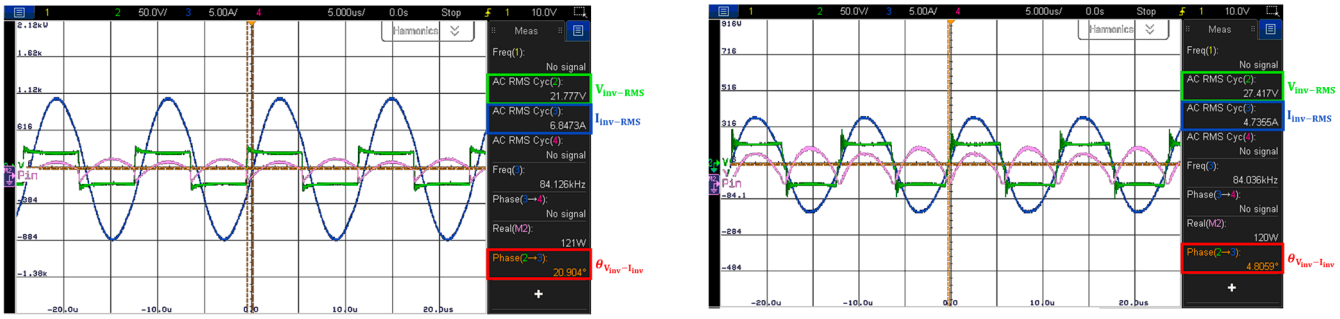

(**a**) (**b**)

Figure 14. Changes in the ZPA of the inverter's output voltage and current based on the method selected for determining resonant capacitance in the WPT system with the SS topology: (**a**) conventional method and (**b**) proposed method.

Table 15 presents the input, output, and PTE values for both the conventional and proposed methods. The abbreviations used for each voltage and current correspond to the symbols used in the circuit diagram of Figure 3. The input and output values summarized in Table 15 represent the DC input and output, respectively. While various previous studies have demonstrated that the conventional resonance method is advantageous for achieving high PTE [10], the proposed method is capable of minimizing leakage magnetic fields while also satisfying the ZPA condition. Specifically, as indicated in Table 15 and Figure 15, the proposed method achieves up to 35% reduction in magnetic field leakage, with only a 2.7% decrease in efficiency. Furthermore, given that the proposed method also helps satisfy the ZPA condition, it can be concluded to be adequately effective.

Table 15. Measured input and output parameters as well as the efficiency of the WPT system with an SS topology.

Parameters	SS Conventional	SS Proposed
V_{in}	30 V	24 V
I_{in}	4.26 A	5.51 A
P_{in} $(= V_{in} \times I_{in})$	127.8 W	132.24 W
V_{out}	28.92 V	28.9 V
I_{out}	3.54 A	3.54 A
P_{out} $(= V_{out} \times I_{out})$	102.4 W	102.3 W
PTE	80.1%	77.4%

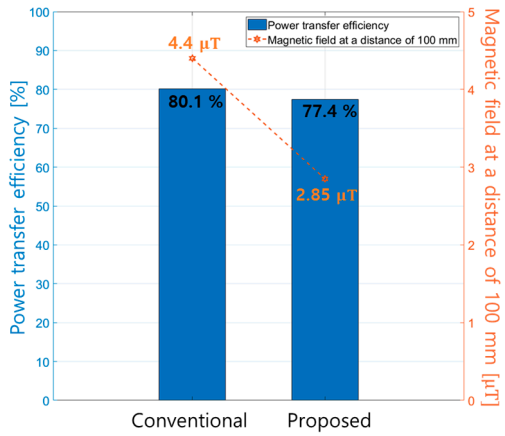

Figure 15. Comparison of the PTE and leakage magnetic field between the conventional and proposed resonance capacitance selection method for the SS topology.

In the initial experimental results, the proposed WPT system achieves an efficiency of approximately 80%, which can be considered relatively low. Upon further analysis, three key factors are identified as contributing to this outcome. First, the optimal load condition is not selected, which is essential for achieving maximum efficiency [28]. Second, the current ratio that yields the highest efficiency is not applied, leading to suboptimal energy transfer [29]. Third, the ferrite structure can be further optimized to enhance magnetic flux control, thus improving the overall efficiency [30]. However, the significance of this study lies in the fact that the proposed system minimizes leakage magnetic fields while satisfying the ZPA resonance condition. Moreover, the system is compared under the same conditions that conventional systems are, making the comparison valid and highlighting the potential of the proposed approach.

Table 16 lists the resonance capacitances used to verify the effectiveness of the proposed method in the WPT system with the double-sided LCC topology. All abbreviations in this table correspond to the symbols used in the circuit of Figure 2. Notably, these capacitances are selected based on Equations (23) and (37) and Table 2. As stated previously, C_{S2} plays a role in minimizing the leakage magnetic field, while C_{S1} determines the ZPA of the WPT system.

Table 16. Resonant capacitances used in the experiment of the WPT system with the double-sided LCC topology.

Parameters	LCC–LCC Conventional	LCC–LCC Proposed
L_{S1}	12.43 µH	
C_{P1}	282 nF	
C_{S1}	141 nF	206 nF
L_{S2}	12.43 µH	
C_{P2}	282 nF	
C_{S2}	141 nF	328 nF

Figure 16 and Table 17 present the measured TX and RX current phase differences and current sum magnitudes for the conventional and proposed resonance capacitance determination methods in the WPT system with the double-sided LCC topology. As indicated in Table 17, when using the proposed method to determine the resonance capacitance, the magnitude of the current sum decreases by up to 46.8% compared to the conventional method. Thus, because the current value, which is the source of the magnetic field, decreases, the leakage magnetic field in the WPT system can also be inferred to decrease.

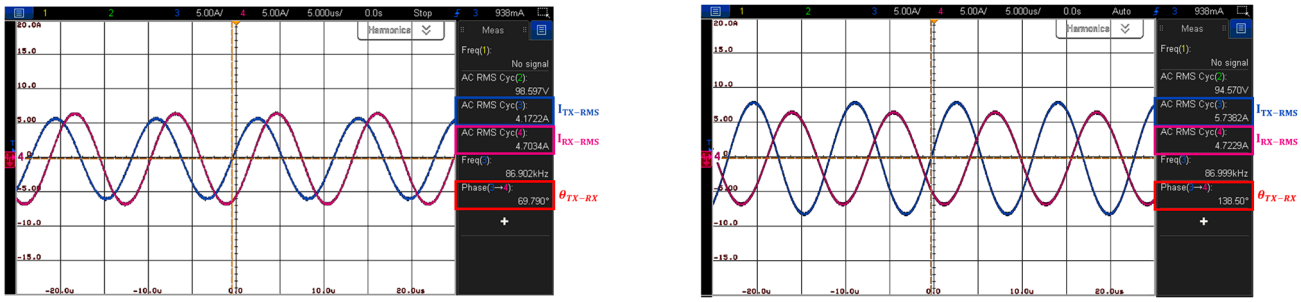

(**a**) (**b**)

Figure 16. Current magnitudes and phase changes as functions of the resonance capacitance values in the WPT system with the double-sided LCC topology: (**a**) when resonance capacitances are selected using the conventional method and (**b**) the proposed method.

Table 17. Magnitudes and phase differences of the current vector sum for the conventional and proposed resonance capacitance determination methods in WPT system with the double-sided LCC topology.

Parameters	LCC–LCC Conventional	LCC–LCC Proposed
$\lvert \mathbf{I_{TX}} + \mathbf{I_{RX}} \rvert$	10.29 A	5.47 A
Phase difference between $\mathbf{I_{TX}}$ and $\mathbf{I_{RX}}$	69.9°	138°

Figure 17 presents the measured magnetic field as a function of the distance from the WPT coil in the system with the double-sided LCC topology. Similar to the experiment for the SS topology, the magnetic field in this experiment is measured in 50-mm increments from 100 to 300 mm. As depicted in Figure 17, when the resonance capacitance is determined using the proposed method, the magnetic field decreases by a maximum value of 42% and a minimum value of 23% compared to when the conventional method is adopted. This reduction aligns with the approximately 46% decrease observed in the total current magnitude, as detailed in Table 17, demonstrating the effectiveness of the proposed method.

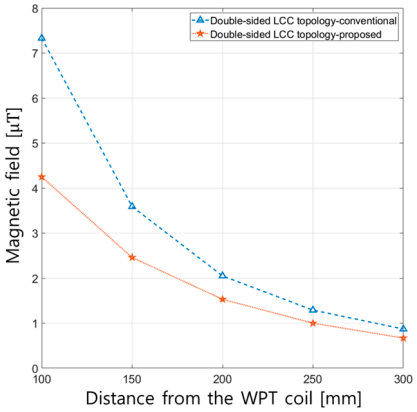

Figure 17. Magnetic field as a function of the distance from the WPT coil when applying the proposed and conventional methods to the WPT system with the double-sided LCC topology.

Next, Figure 18 illustrates the variations in the ZPA characteristics of the WPT system with the double-sided LCC topology depending on the method used to determine the resonance capacitance. Similar to the SS topology, when the resonance of the WPT system with the double-sided LCC topology is tuned using the proposed method, the ZPA characteristics are improved compared to when the conventional method is adopted. Specifically, when the conventional method is used, the voltage–current phase difference at the inverter output reaches 18.4°. Conversely, when the proposed method is adopted, the voltage and current are nearly in phase, with a phase difference of approximately −2.3°.

The experimental results are consistent with the predictions from the analytical equations. After applying the TX resonance capacitance derived from Equations (20) and (41), which satisfies the ZPA condition, the phase difference between voltage and current significantly decreases in the experiments, resulting in improved power transfer efficiency (as shown in Figures 14 and 18). Additionally, after applying the RX resonance capacitances derived from Equations (13) and (32), the experimental results confirm a significant reduction in the leakage magnetic field (as shown in Figures 13 and 17).

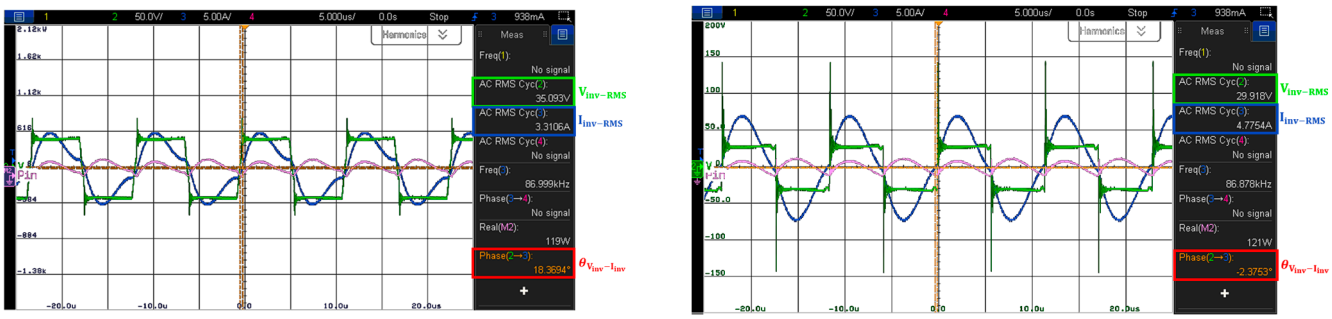

(**a**) (**b**)

Figure 18. Changes in the ZPA of the inverter's output voltage and current based on the method of determining resonant capacitance in the WPT system with the double-sided LCC topology: (**a**) conventional method and (**b**) proposed method.

Finally, Table 18 presents the measured input, output, and efficiency for the WPT system with the double-sided LCC topology. Similar to the SS topology, the PTE for the double-sided LCC topology is approximately 2.5% higher when the resonance capacitance is tuned using the conventional method. Figure 19 compares the leakage magnetic field reduction capability and the PTE performance characteristics of the two methods. Notably, the magnetic field measurement results are based on the values recorded at 100 mm. While tuning the resonance using the proposed method results in a 2.5% decrease in efficiency, it achieves an over 40% reduction in the leakage magnetic field. This highlights the effectiveness of the proposed method, particularly in improving the ZPA characteristics, underscoring its overall utility.

Table 18. Measured input and output parameters and the efficiency of the WPT system with the double-sided LCC topology.

Parameters	LCC–LCC Conventional	LCC–LCC Proposed
V_{in}	31 V	28 V
I_{in}	4.27 A	4.9 A
P_{in} $(= V_{in} \times I_{in})$	132.37 W	137.2 W
V_{out}	29.92 V	29.92 V
I_{out}	3.33 A	3.34 A
P_{out} $(= V_{out} \times I_{out})$	99.6 W	99.9 W
PTE	75.3%	72.8%

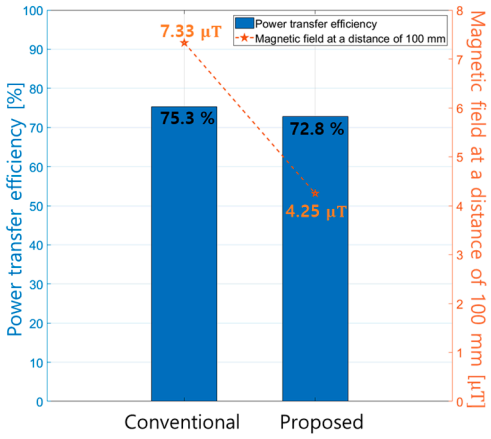

Figure 19. Comparison of the PTE and leakage magnetic field between the conventional and proposed resonance capacitance selection method for the double-sided LCC topology.

4. Conclusions

This study proposed a method for determining resonance capacitance values that could simultaneously improve the ZPA characteristics and minimize the leakage magnetic fields of WPT systems with the SS and double-sided LCC topologies. The necessary equations were derived using a mathematical approach, and the effectiveness of the proposed method was demonstrated through simulations and experiments. The results revealed that the proposed method reduced the leakage magnetic field by up to 35.2% in the SS topology and by 42.0% in the double-sided LCC topology. Furthermore, it improved the ZPA by at least 20° in both cases, highlighting its effectiveness.

The significance of this study lied in the introduction of a practical method for a resonance capacitance selection process suitable for WPT systems, where minimizing leakage magnetic fields was crucial. The findings of this research demonstrated that the proposed method could serve as an optimal solution for resonance tuning in WPT systems.

Although the proposed approach successfully minimized leakage magnetic fields and improved ZPA conditions, some side effects on the system's overall power transfer efficiency (PTE) still remained. Future research could focus on further optimizing the compensation techniques or refining system components, such as ferrite structures and coil designs, to enhance efficiency without compromising performance. Moreover, adaptive control strategies could be developed to dynamically adjust the resonance conditions in real-time, further improving both the efficiency and stability under varying operational conditions.

Author Contributions: Conceptualization, methodology, investigation, and writing, Y.S.; writing—review and editing, and resources, J.R.; and validation, investigation, and supervision, S.W. All authors have read and agreed to the published version of the manuscript.

Funding: This paper was supported by the Korea Institute for Advancement of Technology (KIAT) grant funded by the Korea Government (MOTIE) (P0021513, Industrial Innovation Infrastructure Establishment Project).

Data Availability Statement: The data presented in this study are available on request from the corresponding authors.

Acknowledgments: We would like to acknowledge the technical support from Ansys Korea.

Conflicts of Interest: The authors declare no conflicts of interest.

Appendix A

In the proposed WPT system, a closed-loop control architecture is implemented to dynamically respond to changes in mutual inductance (M) and load resistance (R_{load}). Unlike conventional fixed-parameter systems, this architecture uses real-time sensing and adaptive control to optimize system performance under varying conditions. The system continuously monitors the voltage and current through sensors placed at the TX and RX coils, as well as the load. These measurements are processed to calculate the mutual inductance (M) and detect variations in the load resistance (R_{load}). Based on this information, switch capacitor controllers [31,32] dynamically adjust the resonance capacitors on both the TX and RX sides, allowing the system to continuously switch to resonance capacitors that minimize leakage magnetic fields while satisfying the ZPA condition in real time, despite fluctuations in M and R_{load}.

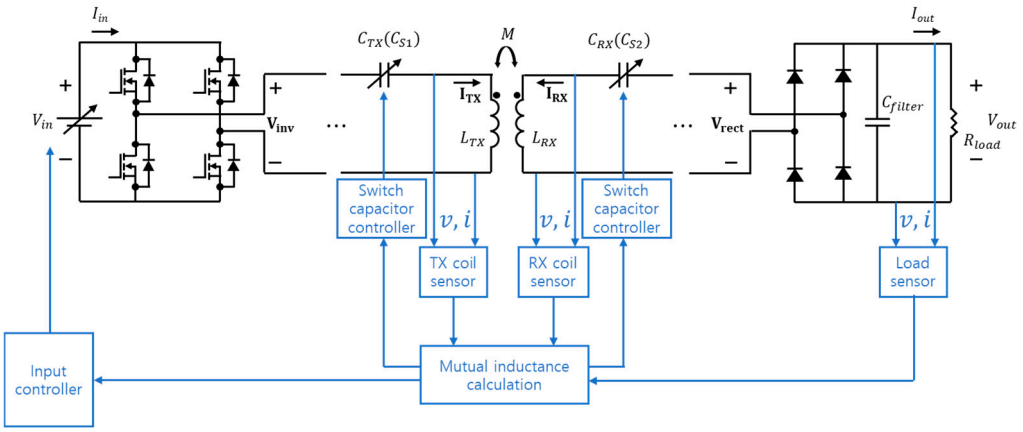

Figure A1. Closed-loop control architecture for real-time adjustment of resonance capacitors in response to changes in mutual inductance and load resistance, minimizing leakage magnetic fields and satisfying ZPA conditions.

The control system is depicted in Figure A1, which illustrates how sensors, controllers, and switchable capacitors interact within the feedback loop to ensure optimal system performance. The input controller also modulates the input voltage, further enhancing the adaptability of the system. By dynamically adapting the resonance condition, the system can achieve higher efficiency and stability compared to conventional systems, which use fixed capacitance values that cannot respond to parameter changes. A comparison between conventional fixed-parameter systems and the proposed adaptive system reveals that the latter offers superior performance when M and R_{load} vary. The dynamic adjustment of the capacitors allows the proposed system to consistently maintain optimal power transfer and minimize reactive power, even in practical scenarios where mutual inductance and load resistance are not constant. This adaptability is critical for real-world applications, such as electric vehicle charging or consumer electronics, where alignment or load conditions can frequently change.

In conclusion, the proposed system's ability to sense and adjust to real-time changes in M and R_{load} represents a significant improvement over traditional methods, offering enhanced efficiency and operational reliability.

References

1. Fernandez-Munoz, M.; Missous, M.; Sadeghi, M.; Lopez-Espi, P.L.; Sanchez-Montero, R.; Martinez-Rojas, J.A.; Diez-Jimenez, E. Fully integrated miniaturized wireless power transfer rectenna for medical applications tested inside biological tissues. *Electronics* **2024**, *13*, 3159. [CrossRef]
2. Allali, N. Enhancing wireless charging for electric vehicles: Active load impedance matching and its impact on efficiency, cost and size. *Electronics* **2024**, *13*, 2720. [CrossRef]
3. De Marcellis, A.; Di Patrizio Stanchieri, G.; Faccio, M.; Palange, E.; Constandinou, T.G. A 6 Mbps 7 pJ/bit CMOS integrated wireless simultaneous Lightwave information and power transfer system for biomedical implants. *Electronics* **2024**, *13*, 1774. [CrossRef]
4. Zouaoui, S.; Dghais, W.; Romba, L.; Melicio, R.; Belgacem, H. Integrated WPT-PLC system applied to UAV: Characterization of a two-coil channel considering misalignment scenarios. *Electronics* **2022**, *11*, 1249. [CrossRef]
5. Wang, J.; Hou, Y.; Shi, Z.; Sun, Q.; Guo, Y.; Cai, S.; Liu, Z. Design and analysis of an H-type pickup for multi-segment wireless power transfer systems. *Electronics* **2024**, *13*, 1125. [CrossRef]
6. Huh, S.; Park, B.; Choi, S.; Shin, Y.; Kim, H.; Kim, J.; Park, J.; Park, D.; Ahn, S. Transmitter coils selection method for wireless power transfer system with multiple transmitter coils and single receiver coil. *IEEE Trans. Power Electron.* **2023**, *38*, 4092–4109. [CrossRef]
7. Shin, Y.; Hwang, K.; Park, J.; Kim, D.; Ahn, S. Precise vehicle location detection method using a wireless power transfer (WPT) system. *IEEE Trans. Veh. Technol.* **2019**, *68*, 1167–1177. [CrossRef]
8. Shin, Y.; Woo, S. Reactive shield for reducing the magnetic field of a wireless power transfer system with dipole coil structure. *Electronics* **2024**, *13*, 1712. [CrossRef]
9. Kim, J.; Kim, J.; Kong, S.; Kim, H.; Suh, I.S.; Suh, N.P.; Cho, D.H.; Kim, J.; Ahn, S. Coil design and shielding methods for a magnetic resonant wireless power transfer system. *Proc. IEEE* **2013**, *101*, 1332–1342. [CrossRef]

10. Huh, S.; Ahn, D. Two-transmitter wireless power transfer with optimal activation and current selection of transmitters. *IEEE Trans. Power Electron.* **2018**, *33*, 4957–4967. [CrossRef]
11. Shin, Y.; Park, J.; Kim, H.; Woo, S.; Park, B.; Huh, S.; Lee, C.; Ahn, S. Design considerations for adding series inductors to reduce electromagnetic field interference in an over-coupled WPT system. *Energies* **2021**, *14*, 2791. [CrossRef]
12. Nguyen, H.T.; Alsawalhi, J.Y.; Hosani, K.A.; Al-Sumaiti, A.S.; Jaafari, K.A.A.; Byon, Y.J.; Moursi, M.S.E. Review map of comparative designs for wireless high-power transfer systems in EV applications: Maximum efficiency, ZPA, and CC/CV modes at fixed resonance frequency independent from coupling coefficient. *IEEE Trans. Power Electron.* **2022**, *37*, 4857–4876. [CrossRef]
13. Zhang, W.; Mi, C.C. Compensation topologies of high-power wireless power transfer systems. *IEEE Trans. Veh. Technol.* **2016**, *65*, 4768–4778. [CrossRef]
14. Lu, J.; Zhu, G.; Lin, D.; Zhang, Y.; Wang, H.; Mi, C.C. Realizing constant current and constant voltage outputs and input zero phase angle of wireless power transfer systems with minimum component counts. *IEEE Trans. Intell. Transport. Syst.* **2021**, *22*, 600–610. [CrossRef]
15. Kim, H.; Kim, J.; Ahn, J.; Shin, Y.; Park, B.; Huh, S.; Choi, S.; Park, J.; Ahn, S. Determination of Compensation Capacitor Considering the Dead-Time Characteristics for ZVS in Wireless Power Transfer System. *IEEE J. Emerg. Sel. Topics Power Electron.* **2023**, *3*, 2501–2513. [CrossRef]
16. Zhu, Y.; Wu, H.; Li, F.; Zhu, Y.; Pei, Y.; Liu, W. A comparative analysis of S-S and LCCL-S compensation for wireless power transfer with a Wide Range load variation. *Electronics* **2022**, *11*, 420. [CrossRef]
17. Trachtenberg, O.; Kuperman, A. Output voltage and resistance assessment of load-independent-voltage-output frequency operating inductive wireless power transfer link utilizing input DC-side measurements only. *Electronics* **2021**, *10*, 2109. [CrossRef]
18. Li, S.; Li, W.; Deng, J.; Nguyen, T.D.; Mi, C.C. A double-sided LCC compensation network and its tuning method for wireless power transfer. *IEEE Trans. Veh. Technol.* **2015**, *64*, 2261–2273. [CrossRef]
19. Vu, V.-B.; Tran, D.-H.; Choi, W. Implementation of the constant current and constant voltage charge of inductive power transfer systems with the double-sided LCC compensation topology for electric vehicle battery charge applications. *IEEE Trans. Power Electron.* **2018**, *33*, 7398–7410. [CrossRef]
20. Corti, F.; Bertolini, V.; Faba, A.; Cardelli, E.; Reatti, A. Design procedures for series–series WPT systems: A comparative analysis. *Comput. Electr. Eng.* **2024**, *119*, 109511. [CrossRef]
21. Park, J.; Shin, Y.; Kim, J.; Park, B.; Kim, H.; Ahn, S. Resonant frequency selection method for wireless power transfer system considering electromagnetic interference reduction. In Proceedings of the 2019 IEEE International Symposium on Electromagnetic Compatibility, Signal and Power Integrity (EMC+SIPI), New Orleans, LA, USA, 22–26 July 2019; pp. 635–638. [CrossRef]
22. Lee, C.; Woo, S.; Shin, Y.; Rhee, J.; Moon, J.; Ahn, S. EMI reduction method for wireless power transfer systems with high power transfer efficiency using frequency split phenomena. *IEEE Trans. Electromagn. Compat.* **2022**, *64*, 1683–1693. [CrossRef]
23. Cruciani, S.; Campi, T.; Maradei, F.; Feliziani, M. Active shielding design for wireless power transfer systems. *IEEE Trans. Electromagn. Compat.* **2019**, *61*, 1953–1960. [CrossRef]
24. Stepins, D.; Zakis, J.; Padmanaban, P.; Deveshkumar Shah, D. Suppression of Radiated Emissions from Inductive-Resonant Wireless Power Transfer Systems by Using Spread-Spectrum Technique. *Electronics* **2022**, *11*, 730. [CrossRef]
25. Inoue, K.; Kusaka, K.; Itoh, J. Reduction in Radiation Noise Level for Inductive Power Transfer Systems using Spread Spectrum Techniques. *IEEE Trans. Power Electron.* **2018**, *33*, 3076–3085. [CrossRef]
26. Hong, S.; Kim, Y.; Lee, S.; Jeong, S.; Sim, B.; Kim, H.; Song, J.; Ahn, S.; Kim, J. A frequency-selective EMI reduction method for tightly coupled wireless power transfer systems using resonant frequency control of a shielding coil in smartphone application. *IEEE Trans. Electromagn. Compat.* **2019**, *61*, 2031–2039. [CrossRef]
27. Zhang, Y.; Yan, Z.; Kan, T.; Zeng, X.; Chen, S.; Mi, C.C. Modeling and analysis of a strongly coupled series–parallel-compensated wireless power transfer system. *IEEE J. Emerg. Sel. Topics Power Electron.* **2019**, *7*, 1364–1370. [CrossRef]
28. Li, X.; Zhang, W.; Si, W.; Wang, R.; Liang, Z. Analysis and Optimization of Equivalent Load for Multichannel Transmission of Wireless Power Transfer. *IEEE Trans. Magn.* **2021**, *57*, 8000906. [CrossRef]
29. Shin, Y.; Woo, S.; Lee, C.; Rhee, J.; Huh, S.; Ahn, S. Determination of Current Ratio to Minimize Power Losses of Coils in Wireless Power Transfer system with Double-Sided LCC Topology. In Proceedings of the 2022 Wireless Power Week (WPW), Bordeaux, France, 5–8 July 2022; pp. 95–98. [CrossRef]
30. Peng, W.; Chen, Z. Enhanced Planar Wireless Power Transfer Systems with Ferrite Material. In Proceedings of the 2018 IEEE Wireless Power Transfer Conference (WPTC), Montreal, QC, Canada, 3–7 June 2018; pp. 1–4. [CrossRef]
31. Khan, S.A.; Ahn, D. Automatic Resonance Tuning With ON/OFF Soft Switching for Push–Pull Parallel-Resonant Inverter in Wireless Power Transfer. *IEEE Trans. Power Electron.* **2022**, *37*, 10133–10138. [CrossRef]
32. Luo, Z.; Zhao, Y.; Xiong, M.; Wei, X.; Dai, H. A Self-Tuning LCC/LCC System Based on Switch-Controlled Capacitors for Constant-Power Wireless Electric Vehicle Charging. *IEEE Trans. Ind. Electron.* **2023**, *70*, 709–720. [CrossRef]